

Detailed experimental and theoretical study of collision-induced dissociation of Na_2^+ ions on He and H_2 targets at keV energies

J. A. Fayeton, M. Barat, J. C. Brenot, H. Dunet, and Y. J. Picard

Laboratoire des Collisions Atomiques et Moléculaires (URA D 0281), Université Paris-Sud, 91405 Orsay Cedex, France

U. Saalmann

Max-Planck-Institut für Physik komplexer Systeme, Nöthnitzer Straße 38, 01187 Dresden, Germany

R. Schmidt

Institut für Theoretische Physik, Technische Universität Dresden, 01062 Dresden, Germany

(Received 1 August 1997)

A combined experimental and theoretical investigation of collision-induced dissociation (CID) of the quasi-one-electron system $\text{Na}_2^+ \text{He}$ at 80 eV center-of-mass energy is presented. This study, complemented by additional measurements with an H_2 target, provides a detailed analysis of the competition between the two basic CID mechanisms: via excitation of electronic states of the Na_2^+ molecular ion and via momentum transfer to one of the Na^+ core. The experimental method is based on a combined coincidence and time-of-flight technique, resulting in a complete measurement of the velocity vectors of the two fragments and giving a full determination of the collision parameters. The theoretical analysis is based on the so-called nonadiabatic quantum molecular dynamics, developed recently. This theory treats self-consistently and simultaneously classical atomic motion and quantum electronic transitions in dynamical processes of atomic many-body systems using time-dependent density functional theory. It allows one to simulate the experiment in microscopic detail and, thus, provides a deep insight into the excitation and dissociation mechanism. The combined theoretical and experimental analysis can later be extended to more complex systems like larger molecules or clusters. [S1050-2947(98)04602-2]

PACS number(s): 34.50.Pi, 34.10.+x, 36.40.Qv

I. INTRODUCTION

Collision-induced dissociation (CID) of a diatomic molecule is a simple example of the dynamics of a finite system. It is noticeable that no complete analysis of such a simple “three-body” collision process has been realized yet, while research in this field has been vigorous for decades [1]. Study of CID was initiated in the 1960s when it was suggested that dissociation of H_2^+ could be a means to produce fast H beams to heat plasmas of interest for fusion. Then an intense activity developed in spectroscopy when it was realized that velocity measurements of ionic fragments coming from the dissociation of fast (10 keV) molecular ions could provide information on molecular energy levels with meV accuracy owing to the magnification of the energy of the fragments introduced by the-laboratory-to-center-of-mass transformation [2]. This “translational spectroscopy” was later extended by detecting the two fragments in coincidence [3]. With this technique, spectroscopy of highly excited molecules could be studied for the first time. But, concerning the understanding of the collision dynamics, unavoidable integration on several variables necessitates the use of models to disentangle the complex data. A first assumption, which applies well to the present energy range, comes from the comparison of some characteristic times: the collision time, typically 10^{-16} – 10^{-15} s, is at least one order of magnitude shorter than the vibration time, itself two orders of magnitude shorter than the rotation time. This allows one to consider a “two-step” mechanism: first the molecule is excited into an unstable state by the collision, then, in a second step,

the molecule dissociates far from the perturber. For the first step, two different collision mechanisms have been considered depending on whether the perturber interacts primarily with the nuclear cores or with the electronic cloud of the molecule:

(i) In the first type of interaction, also called rovibrational dissociation [1], the target atom exchanges momentum with one or both atomic cores of the molecule resulting in a stretching of the molecular bond and vibrational excitation [4]. If the momentum transfer is large enough, dissociation occurs. In the simplest situation, the momentum is transferred in a close encounter with one atomic core resulting in a significant deflection of the center of mass (CM) of the molecule. This mechanism, hereafter referred to as the *impulse mechanism* (IM), although often invoked, was never directly observed. Actually, with the available techniques, it was not possible to measure enough variables for a given event to determine the scattering angle, as will be discussed in this paper.

(ii) The *electronic mechanism* (EM) involves excitation of the molecule into a dissociative state. At low collision energy, in the so-called “quasimolecular” regime, direct electronic excitation is usually small. In contrast, electron capture might be a very important electronic process, provided that quiresonant conditions are fulfilled. In this situation electron capture takes place at large impact parameter, leading to large geometrical cross sections and a forward scattering of the fragments. Since rotation is usually very slow, one generally assumes that dissociation takes place along the internuclear axis (“the axial recoil assumption”) [5]. Dissocia-

tive [6] or predissociative [7] states of various molecules have then been investigated, these states being formed via resonant electron capture by their parent ions colliding with alkali targets. The analyzing technique makes use of the negligible deflection of the CM of the molecule, allowing a complete determination of the momentum distribution from the only measurements of the difference of arrival times and the distance of the two fragments detected in coincidence on a position-sensitive detector [3].

These two mechanisms are invoked in many other processes. For example, IM can mediate reactive processes [8] whereas EM is essentially that of the photodissociation. More generally, IM and EM are nothing but the electronic and nuclear components of the "stopping power" of atomic particles inside the bulk. This motivated the present experimental (see [9] for a preliminary account) and theoretical study of the competition between these two basic CID mechanisms at low collision energy. From the experimental side, a full determination of the velocity vectors of the two fragments (measurement of the six velocity components) gives a complete analysis of the CID. In particular, the deflection angle of the dissociated molecular ion can be recovered. The collision of Na_2^+ ions with He and H_2 targets has been chosen for the following reasons: the heavy projectile light target combination allows an almost complete collection of all fragments on the detectors, hence realizing a 4π detector in the center of mass. Only a few events are missed for large scattering angles with He target. This would not have been the case for example, with a H_2^+ beam. This is also one of the simplest systems since only the $\sigma_g 3s$ electron of Na_2^+ is expected to be active at these energies, while the strongly bound target electrons should not participate to the process. In particular charge exchange was not expected and indeed not observed. This simple system thus provides a case study for testing the nonadiabatic quantum molecular dynamics theory recently developed by Saalman and Schmidt [10].

II. EXPERIMENT

A. Experimental setup (Fig. 1)

The Na_2 dimers are produced in gas phase through a neat expansion of pure sodium vapor. The oven is a double chamber made of stainless steel 310, consisting of a large backing oven and a small frontal nozzle device. The backing oven is typically operated at a temperature ranging from 650 to 850 °C corresponding to vapor pressures of 50 to 500 Torr, respectively. The sonic nozzle of 0.125 mm diameter is located 18 mm in front of a conical heated skimmer. The distance between the nozzle and the skimmer as well as the transverse position of the oven can be adjusted to optimize the Na_2^+ intensity.

The sodium beam passing through a ring-shaped filament is ionized by 40-eV electrons. The ions are then accelerated at the desired energy of 1 keV and steered towards the entrance hole of a Wien filter. The Na_2^+ beam is mass selected by passing through an exit hole located at 900 mm (both holes have a 1 mm diameter) and chopped at 1 MHz in a parallel plate condenser with a 0.8-V/mm electric field, resulting in 10-ns-wide pulses. A third circular hole limits the beam diameter to 0.5 mm with an angular aperture of 0.2° .

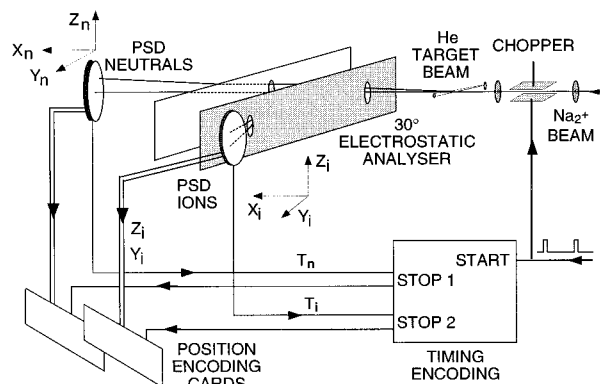


FIG. 1. Experimental setup.

Finally the molecular ion beam crosses at 90° a He or a H_2 thermal target beam issued from a supersonic expansion designed by Campargue [11]. The use of a "cold" target drastically reduces the velocity broadening in the scattered beam especially important in heavy projectile light target combinations. The beam-crossing region determines a cylindrical collision volume of about 1.5 mm long and 0.5 mm diameter, which is placed at the focus point of a 30° parallel plate electrostatic analyzer. This device is primarily used to separate the neutral fragments from the ionic ones and to mass select these ionic fragments. The Na^+ ions are received on a 40-mm-diameter position-sensitive detector (PSD) placed at an angle of 11° in the image plane of the analyzer [12]. This arrangement also allows to use the electrostatic analyzer to measure the energy of the incident and scattered ions. The neutral fragments fly straightforwardly through a fine mesh grid stretched on the outer plate of the analyzer and reach a second PSD located in the incident beam direction. Each PSD is constituted by a stack of 3 microchannel plates (Hamamatsu F 1217-01) and a resistive anode (Quantar Technology Inc. 1839). The Y and Z positions of both neutral and ionic fragments are determined by the charge division technique: the charges at the four corners of the collectors are amplified, discriminated, and converted into 12 bits data with two "Datel" (PC-414A2) cards featuring four "sample and hold" devices simultaneously triggered by the timing signal. The typical 0.1-mm spatial resolution of the PSD corresponds to an 0.01° angular resolution much better than the angular spread of the incident beam (0.2°). The size of the PSD actually limits the angular acceptance of the neutral fragments to 3.2° . For ion fragments, the limiting angle is 3° in the Z direction (Fig. 1) but the focusing properties do not practically limit the acceptance in the Y direction.

In order to simultaneously determine the velocity vectors of both Na and Na^+ fragments issued from the same physical event, times of flight (TOF) of both fragments detected in coincidence are measured by a multihit, multistop time digitizer (CTNM2 manufactured by IPN Orsay) triggered by the chopper clock. Data are recorded in the "event" mode: for each event occurring in a period of 256 μs , the positions Y , Z (12 bits) as well as the TOF (0.5-ns accuracy) of both fragments are recorded.

The energy spread of the incident beam measured by the electrostatic selector was found to be 2 eV approximately at 1000 eV. The accuracy of the measurements is primarily

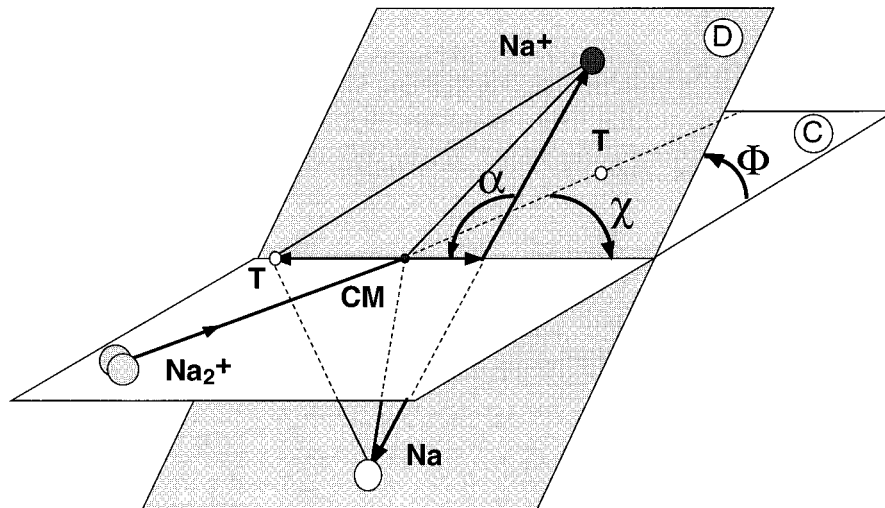


FIG. 2. Parameters defining the collision geometry: C is the collision plane defined by the incident and recoil velocity vectors of the target (T) in the $\text{Na}_2^+ - T$ center-of-mass (CM) frame. χ is the CM scattering angle. D is the dissociation plane, which makes an angle Φ with C . $\Phi < 90^\circ$ corresponds to a forward scattering of the ion. α is the angle between the relative velocity of the fragments (the $\text{Na}-\text{Na}^+$ vector) and the target recoil velocity.

limited by the time width of the beam, which is typically 10 ns for a total flight of about 5 μs .

B. Data analysis

The velocity vector \mathbf{V}_n of the neutral fragment is determined by the three spatial coordinates X_n, Y_n, Z_n and by the time T_n spent by the Na atom between the collision volume and the neutral PSD ($X_n = 348.5 \pm 0.5$ mm). Y_n and Z_n are given by the location of the fragment on the PSD. The main uncertainty comes from the determination of the $Y_n = Z_n = 0$ origins obtained from the assumed cylindrical symmetry of the scattered neutral (noncoincident) fragments. The accurate determination of T_n is more difficult. In a first step, we let the incident ion beam strike at reduced intensity the neutral PSD. This gives a time reference peak t_{ref} . The actual TOF of the incident beam T_{ref} is calculated from the ion velocity determined by its kinetic energy eV_0 given by the voltage supply and by the flight path X_n . The time $T_n = T_{\text{ref}} + (t_n - t_{\text{ref}})$ is then determined from the measurement of the arrival time t_n of the neutral fragment with respect to t_{ref} . Anticipating the results, the consistency of the method has been verified using the location of structure III (see next section). This method allows one to bypass problems encountered with absolute timing such as delays given by electronics, wiring, and chopping method. The same procedure is used to determine the TOF T_i of the ionic fragment, from which the vector \mathbf{V}_i is determined. In fact $T_i - T_n$ is obtained with a 0.5-ns accuracy given by the time digitizer and does not suffer from the errors introduced in the T_{ref} definition. The ionic trajectories between the collision volume and the X_i coordinate of the ion impact on the PSD are calculated assuming a uniform electric field inside the analyzer and zero field outside. Small corrections are then added to recover the cylindrical axial symmetry of the (noncoincident) scattered ions. Once the \mathbf{V}_n and \mathbf{V}_i vectors are determined for all coincident events, the data are presented in coordinates that are better adapted to the present collision problem (Fig. 2). An important aspect concerns the choice of the most pertinent

parameters, and when chosen, the most significant correlation between them. The CM scattering angle χ , which is also the recoil angle of the target, is one of them; it allows one to appreciate how violent the collision is. The other parameters are E_{rel} , the relative kinetic energy of the fragments, α and Φ , the two angles determining the orientation of the dissociation axis.

III. EXPERIMENTAL RESULTS

All data presented in this paper have been obtained at a laboratory energy of 1000 eV corresponding to 80-eV CM for a He target and to 41.7 eV CM for a H_2 target. In order to pinpoint the similarities and differences between the two systems, we have chosen to present the data obtained with both helium and H_2 targets together. Actually one of the most significant correlations is provided by the dependence on χ of E_{rel} as shown in Fig. 3. It is noteworthy that both systems present a similar pattern composed of three structures. Integration for each structure of the multiply differential cross sections gives for structures I, II, and III relative contributions of 68%, 17%, and 14% with the He target and 51%, 33%, and 16% with H_2 , respectively. Structures II and III appear at very small scattering angle, corresponding to gentle collisions. They are attributed to electronic transitions to repulsive (structure II) or weakly bound (structure III) states. They will be discussed later. In contrast, the structure labeled I appears at large χ values. With both targets, E_{rel} increases with χ , but with different origin and slope. This behavior suggests that structure I is due to an impulse mechanism. Considering a binary collision between the target and one Na^+ core, a larger χ would correspond to a larger momentum transfer and therefore to a larger relative energy of the fragments.

A. Impulsive processes

In order to check the cogency of this assumption, one has developed a simple binary model, in which we assume an

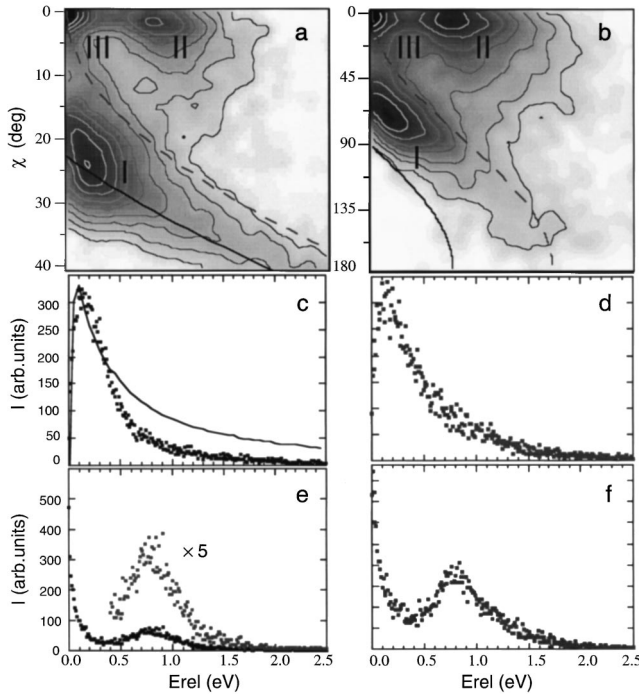


FIG. 3. Contour maps for the correlation between the relative kinetic energy of the fragments E_{rel} and the CM scattering angle χ for (a) helium target and (b) H_2 target in the Na_2^+ -He and Na_2^+ -H CM frames, respectively, (see text). All contour levels show a logarithmic intensity scale with a factor of 1.58 between two contours. Impulse model: full lines: $E_{\text{int}}=0$, dotted lines: $E_{\text{int}}=0.96$ eV. The middle and lower panels show the intensity as a function of E_{rel} for process I: (c) $\chi > 10^\circ$ for the He target, (d) $\chi > 25^\circ$ for the H_2 target and processes II and III: (e) $\chi < 10^\circ$ for He target, (f) $\chi < 25^\circ$ for H_2 target, respectively. The full line in (c) stands for the model calculation taking the rotation of the dissociation axis into account (see text).

elastic encounter between one Na^+ core and the target, neglecting the interaction with the other core. The active Na^+ is scattered at an angle χ_1 in the frame of the Na^+ target center of mass (Fig. 4). In this frame, its velocity vector becomes BA' , while BA remains that of the untouched Na^+ . AA' is the velocity transferred to the relative motion of the

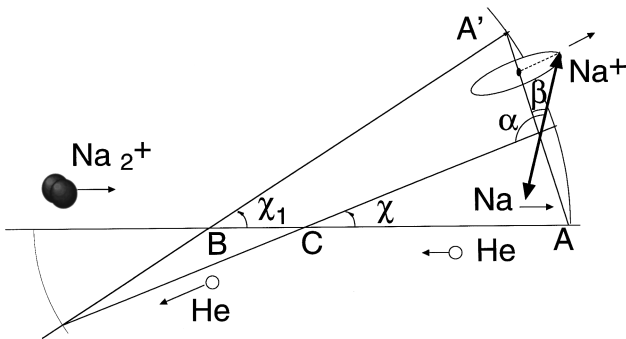


FIG. 4. Newton diagram for the binary impulse model for the Na_2^+ -He system: B: Na-He CM, C: Na_2 -He CM, χ_1 scattering angle in the Na^+ -He CM frame. AA' is the dissociation velocity vector if the two Na^+ cores were not bound. β is the angle between the actual dissociation velocity Na-Na $^+$ vector and the direction of the transferred momentum.

two Na^+ cores. If the corresponding energy transfer E_T is larger than the binding energy of Na_2^+ , the molecule dissociates with

$$E_{\text{rel}} = E_T - E_D + E_{\text{int}},$$

where E_{int} is the rovibrational energy of the incident Na_2^+ ion and $E_D = 0.96$ eV is the ground-state binding energy. The dependence of E_{rel} on the CM scattering angle χ can easily be calculated (Fig. 4) with

$$E_T = \frac{M_T^2}{(M_T + M_{\text{Na}})^2} E_0 \sin^2 \frac{\chi_1}{2},$$

$$\tan \chi = \frac{\sin \chi_1}{M_T / (M_T + 2M_{\text{Na}}) + \cos \chi_1},$$

where M_T and M_{Na} are the target and Na masses, respectively. The initial rovibrational energy E_{int} of Na_2^+ being unknown, the $E_{\text{rel}}(\chi)$ curves have been drawn for the two limit values $E_{\text{int}}=0$ and $E_{\text{int}}=0.96$ eV corresponding to Na_2^+ in the rovibrational ground state and at the dissociation limit, respectively (see Sec. IV: Fig. 14). It is noteworthy that for the He target [Fig. 3(a)] the experimental contours follow surprisingly well the curves in view of the crudeness of the model. The maximum of the experimental data lies between 0 and 0.2 eV above the lower curve. This gives an estimate of the initial internal energy of the Na_2^+ projectile. Assuming that at an oven temperature $T=800^\circ\text{C}$, only $v=0,1,2$ vibrational states are populated. Therefore the ionization resulting from a Franck-Condon transition from these states gives an internal energy $E_{\text{int}} < 0.2$ eV consistent with our estimate. In the case of the H_2 target, a binary encounter of one H atom with one Na^+ core has been considered since the IM involves a hard collision that can only occur between atomic cores. A glance at Fig. 3 shows again a good agreement with the experimental contours, an agreement that is not found if a collision with H_2 instead of H was considered. For consistency, the experimental data have been presented in the Na_2 -H CM frame. Notice that a simple binary Na^+ -H collision governs, to a large extent, the dissociation dynamics of such a four-body system. It is interesting to notice that in the Na^+ -H binary encounter, the energy simultaneously transferred to H_2 ($E'_T = E_T M_{\text{Na}} / M_{\text{H}}$) is 23 times larger than that given to Na_2^+ . That means that H_2 should simultaneously dissociate in this process since the energy transferred to H_2 as Na_2^+ dissociates is at least 22 eV ($E_{D_{\text{H}_2}} = 4.47$ eV).

The $I(E_{\text{rel}})$ distribution for structure I, integrated over angles $\chi > 10^\circ$ [Fig. 3(c)] peaks at a relative E_{rel} value around 0.12 eV, a feature not expected from the model that predicts a maximum for $E_{\text{rel}} \rightarrow 0$ eV. It is suggested that this shift of the maximum is introduced by a centrifugal barrier E_{cfg} to be overcome during the dissociation of the rotationally excited Na_2^+ (Fig. 5). The above model has therefore been complemented to account for the part of the momentum transmitted to the rotational degrees of freedom. For each χ angle and E_{rel} values, the differential cross section is then given by

$$\sigma_{\text{rot}}(\chi, E_{\text{rel}}) = \sigma(\chi) P(\chi, E_{\text{rel}}) P_{\text{cfg}}(\chi, E_{\text{rel}}).$$

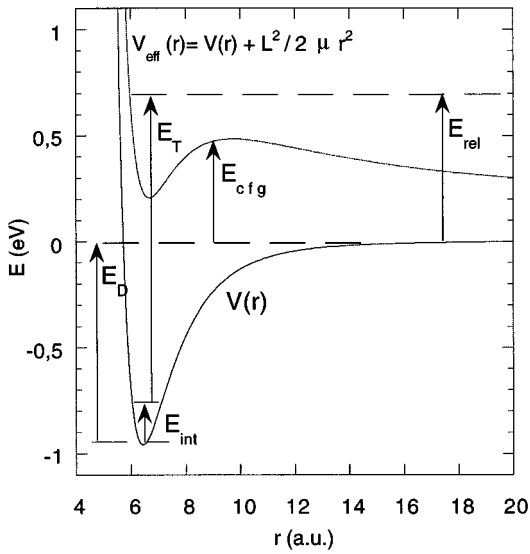


FIG. 5. Schematic representation of the rotational barrier. See text (Sec. III A) for the definitions of the various energies. $V_{\text{eff}}(r)$ is the sum of the Na_2^+ potential $V(r)$ and the centrifugal potential.

$\sigma(\chi)$ is the differential cross section corresponding to the first binary elastic Na^+ -He collision, calculated with the potential given by Kita *et al.* [13]. $P(\chi, E_{\text{rel}})$ is the distribution of the internal energy of Na_2^+ , which is assumed to be a Gaussian curve centered at $E_{\text{int}} = 0.2$ eV with a half width at half maximum (HWHM) of 0.3 eV (see Sec. III A). $P_{\text{cfg}}(\chi, E_{\text{rel}})$ accounts for the barrier height: $P_{\text{cfg}} = 0$ or 1 depending whether E_{rel} is smaller or larger than E_{cfg} respectively. Such calculation is performed for all orientations between the Na_2^+ axis and the momentum transfer axis by steps of 10° . The differential cross section averaged over these orientations is then, for each E_{rel} value, summed over scattering angles χ . The reasonable agreement with the experimental data for the shift of the maximum [Fig. 3(c)] supports our assumption on the role of the rotational transfer.

Within this model, the momentum is transferred in the collision plane, implying that the dissociation fragments are emitted symmetrically with respect to this plane. The $\Phi(\chi)$ correlation (Fig. 6) shows the strong peaking of the experimental data for process I at $\Phi = 0^\circ$ and $\Phi = 180^\circ$ around the collision plane, also in consistency with the model. With the He target an asymmetry in the Φ distribution is found for $\chi > 30^\circ$. In fact, for these large angles, a significant part of the side scattered neutral fragments falls outside the PSD (see Sec. II) explaining the absence of coincidences at $\Phi = 0^\circ$, even though the corresponding ionic fragments are detected. The hatched areas in Fig. 6(a) show the part of the (χ, Φ) plane that is at least partially blind to neutral fragments. On the contrary, at $\Phi = 180^\circ$ and large χ most of the side scattered ionic fragments are detected, explaining the observed peaking of the coincident data. However, with the H_2 target, such an angular cut does not occur due to the lower target-projectile mass ratio. Therefore the neat asymmetry in the relative intensities at $\Phi = 0^\circ$ and 180° must have a physical origin at variance with the He case. This asymmetry is not expected from the two-step approximation in which first the target hits one Na^+ core and then, in the

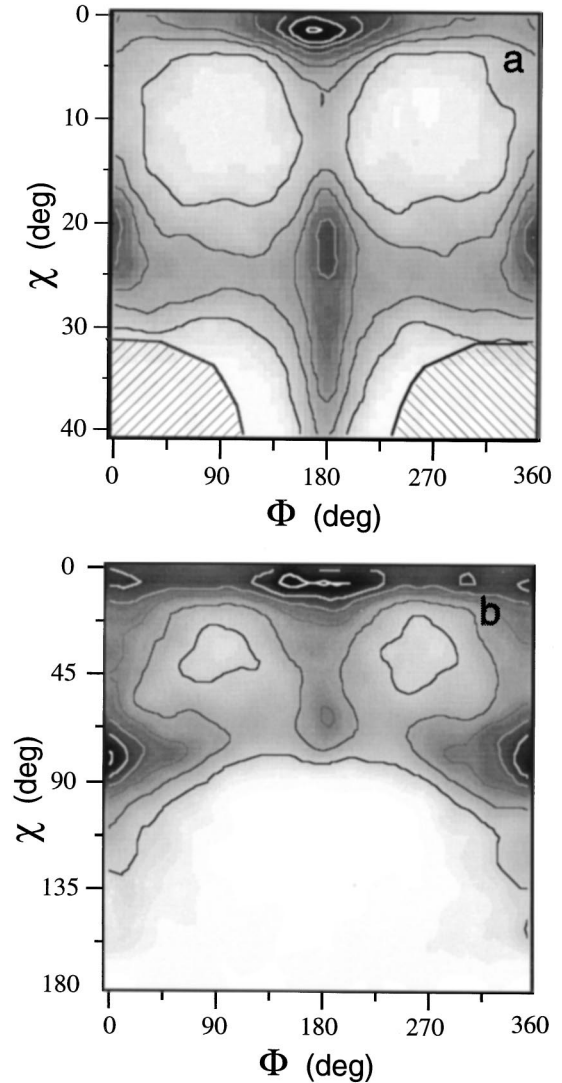


FIG. 6. Contour maps for the correlation between the CM scattering angle χ and the angle Φ between the collision and the dissociation planes for (a) He and (b) H_2 in the Na_2^+ -He and Na_2^+ -H CM frames, respectively (see text). All contours show a linear plot with a factor 2 between two contours. The hatched areas stand for the part of the (χ, Φ) plane at least partially blind to the neutral fragments in the case of the He target.

second step, the molecular ion dissociates far from the perturber. The active σ_g $3s$ electron has therefore an equal chance (due to the molecular symmetry) to be bound to either a Na^+ ion, resulting in an equal probability to detect a Na or Na^+ fragment at a given scattering angle. The clear departure from such symmetry in the case of the H_2 target may put in question the limit of the two-step assumption. ‘‘Postcollision’’ interaction with the target could be invoked, an interaction that is much stronger with H_2 (or H if H_2 dissociates as suggested above) than with He possibly due to the larger polarizability (0.8, 0.67, and 0.2 \AA^3 , respectively). An alternative explanation implies the excitation of the Na^+ $2p$ core electrons in close Na^+ -H encounters, breaking the Na^+ - Na^+ core symmetry. This excitation process is much less important in Na^+ -He encounters. For example, this mechanism has been observed in the dissociation of the asymmetric NaK^+ ion [14].

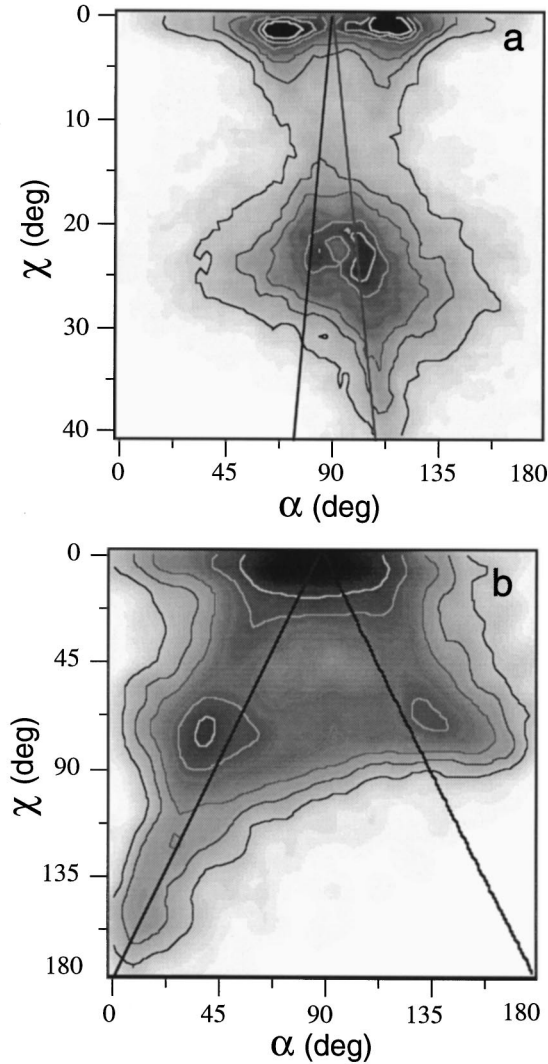


FIG. 7. Contour maps for the $\alpha(\chi)$ correlation for (a) He and (b) H_2 in the Na_2^+ -He and Na_2^+ -H CM frames, respectively (see text). Same scale of contours as in Fig. 6. The two lines are the $\alpha = \pi/2 \pm (\chi - \chi_1/2)$ values given by the impulse model.

The α angle gives the orientation of the dissociation axis with respect to the scattered beam axis. Within the impulse model, a simple relationship is found between χ_1 and χ angles (Fig. 4): $\alpha_0 = \pi/2 \pm (\chi - \chi_1/2)$ depending on whether the ion or the neutral fragment is side scattered by the target. The dotted lines well account for the double peaking of the $\alpha(\chi)$ data (Fig. 7). A more sensitive parameter is the angle $\beta = \alpha - \alpha_0$ (Fig. 4) between the direction of the momentum transfer and the actual dissociation axis. Figure 8 shows the correlation $\beta(E_{\text{int}})/\sin\beta$. The $\beta(E_{\text{int}})$ data have been divided by $\sin\beta$ in order to suppress the effect of the spherical coordinates, which artificially privileges data at $\beta=90^\circ$ [15]. One notices again the strong peaking around $\beta=0^\circ$ and $\beta=180^\circ$ along the momentum transfer axis. It is readily seen that the larger the initial vibrational energy, the better the model applies, as it was expected in a model that neglects the interaction with the untouched Na^+ core.

B. Electronic processes

The energy loss measurements and the very small $E_{\text{rel}}(\chi)$ values suggest attributing structure III to the population of

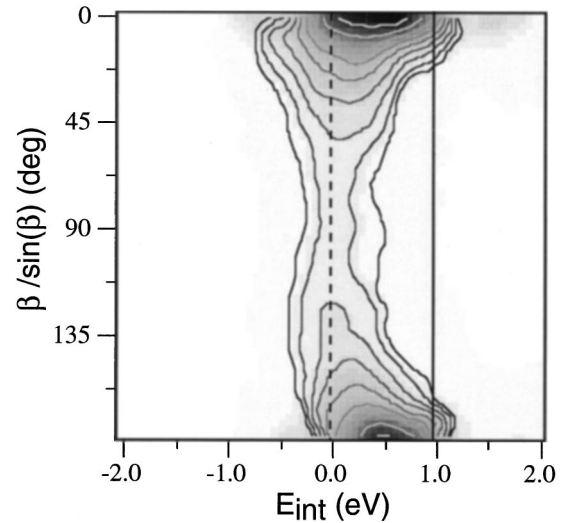


FIG. 8. Contour map for the correlation between the angle $\beta/\sin\beta$ and the internal energy E_{int} of Na_2^+ (see text). Same scale of contours as in Fig. 3. The dashed and full lines are for an internal energy of 0 and 0.96 eV, respectively.

weakly bound states correlated to the $\text{Na}(3p) + \text{Na}^+$ dissociation limit but does not allow one to distinguish between the two possible $\sigma_g 3p$ or $\pi_u 3p$ channels (see Sec. IV: Fig. 14). The Φ and α angular distributions are also very difficult to estimate due to the strong peaking around $E_{\text{rel}}=0$ eV and $\chi=0^\circ$. Nevertheless, for the He target, the α distribution is peaked around $\alpha=\pi/2$ (Fig. 9) and looks very close to a $\sin\alpha$ shape (see Sec. IV: Fig. 16) as expected from a uniform distribution of the dissociation axis. In contrast, a clear asymmetry towards the small α values is observed with H_2 . Complementary measurements made after our preliminary analysis [9] show that structure II is primarily due to the dissociation of the $\sigma_u 3s$ repulsive state (see Sec. IV). The energy distribution of the fragments $I(E_{\text{rel}})$ peaks around 0.7 eV [Figs. 3(e) and 3(f)] a value that would correspond to a transition around 8.5 a.u. assuming a Frank-Condon transition. The α angular distribution shows a double structure peaking at 70° and 110° for the He target and 80° and 100° for H_2 , symmetric around $\alpha=\pi/2$. Notice that for H_2 the $\alpha(E_{\text{rel}})$ plot is presented in the Na_2 - H_2 CM frame at variance with the previous plots, which referred to the binary Na-H encounter. These two peaks actually correspond to the same orientation of the dissociation axis just exchanging the Na and the Na^+ fragments. The α distribution becomes closer to $\alpha=\pi/2$ with increasing E_{rel} . This behavior could reflect the dependence of the cross section on the internuclear distance (related here to E_{rel}) at which the transition occurs as discussed by Green and Peek [16] for the CID of H_2^+ . The determination of the $I(\Phi)$ distribution (Fig. 6) at very small scattering angles is rather sensitive to various experimental parameters and this distribution even becomes meaningless at $\chi=0^\circ$. In this respect, the strong peaking at $\Phi=180^\circ$ should not be considered as significant. However, with increasing χ up to 10° the meaningful double peaking at $\Phi=0^\circ$ and $\Phi=180^\circ$ shows a preferential in-plane dissociation for both II and III structures and with both targets. This clearly indicates that some momentum might be simulta-

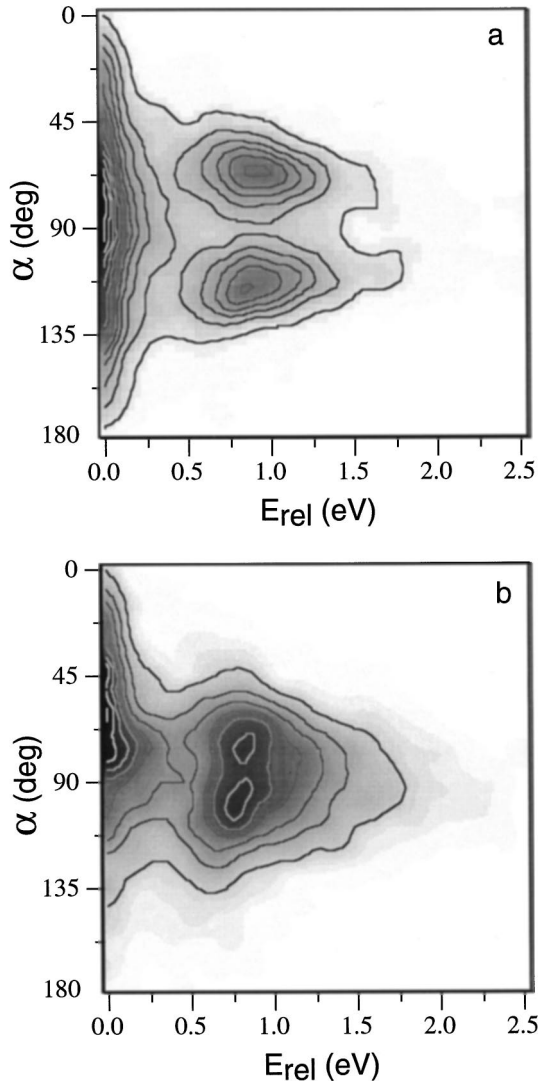


FIG. 9. Contour maps for the $\alpha(E_{\text{rel}})$ correlation for (a) He target and (b) H_2 target corresponding to electronic processes I and II ($\chi < 10^\circ$). Notice that for such electronic processes the $\alpha(E_{\text{rel}})$ correlation is presented in the Na_2^+ -He and Na_2^+ - H_2 CM frames, respectively (see text). Same scale of contours as in Fig. 6.

neously transferred during EM for rather close encounters between the target and one of the Na^+ cores (see Sec. IV).

C. The “ZZ correlation”

Actually, information on the type of dissociation mechanism can be obtained from the correlation between the positions of the two fragments, in fact their projection on the vertical axis Z , with respect to the incident beam axis (Fig. 10). The ZZ correlation does not require timing measurements and thus can be obtained with a continuous beam. A factor of 100 is thus gained in the beam intensity with respect to the chopped beam procedure, a feature that is appreciated when working with weak cluster beams [17,18]. For the electronic mechanism, the scattering of the CM of the molecular ion is negligible: if the ionic fragment is deflected up, the neutral fragment is deflected down, and conversely. This process gives the body of the “butterfly” pattern in the ZZ correlation. In an impulsive mechanism, a hit core,

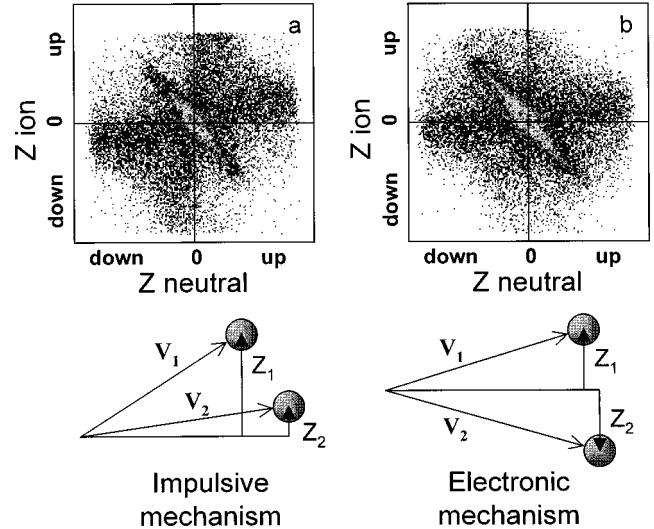


FIG. 10. ZZ correlations for (a) He target and (b) H_2 target. Abscissa and ordinate are the vertical components of the deflection of the neutral and the ionic fragments, respectively. Lower panel: schematic ZZ topology for impulsive and electronic mechanisms.

ejected as a neutral fragment, for example, is much more deflected than the passive fragment, which, however, is slightly deflected in the same side due to the molecular binding. The corresponding ZZ correlation gives the horizontal wing of the butterfly, while the vertical wing corresponds to a hit fragment ejected as an ion. The integration of the scattered intensity shows for the H_2 target an increasing importance of the EM and a decrease of the vertical wing showing up the asymmetry in the IM (see Sec. III A).

IV. THEORETICAL ANALYSIS

In this section we present a detailed theoretical analysis of the $\text{Na}_2^+ + \text{He}$ ($E_{\text{CM}} = 80$ eV) collision system. It is based on the so-called nonadiabatic quantum molecular dynamics (NA-QMD) developed recently [10]. This theory treats simultaneously and self-consistently classical atomic motion and electronic transitions (excitation, transfer, ionization) in atomic many-body systems by combining classical molecular dynamics with time-dependent density functional theory. The general equations of motion as well as approximations to make the approach applicable to larger systems are discussed in [10]. Technical details of the calculations presented in this application will be published elsewhere [19].

The aim of the present theoretical analysis is twofold: *First*, the comparison of the calculated results with that of full-kinematic correlation experiments represents a sensitive test of the NA-QMD theory. *Second*, a NA-QMD analysis allows one to obtain a detailed microscopic insight into the excitation and dissociation mechanisms by considering also non-measurable quantities such as time and impact parameter dependence of different processes.

So, we have performed a systematic event-by-event analysis of the collisions $\text{Na}_2^+ + \text{He}$ by calculating about 35 500 trajectories with the NA-QMD covering 71 impact parameters ($b = \sqrt{k/2}$ a.u. with $k = 0, 1, \dots, 70$) and 500 initial conditions, i.e., different orientations of the cluster with respect to the beam axis for each impact parameter. In addi-

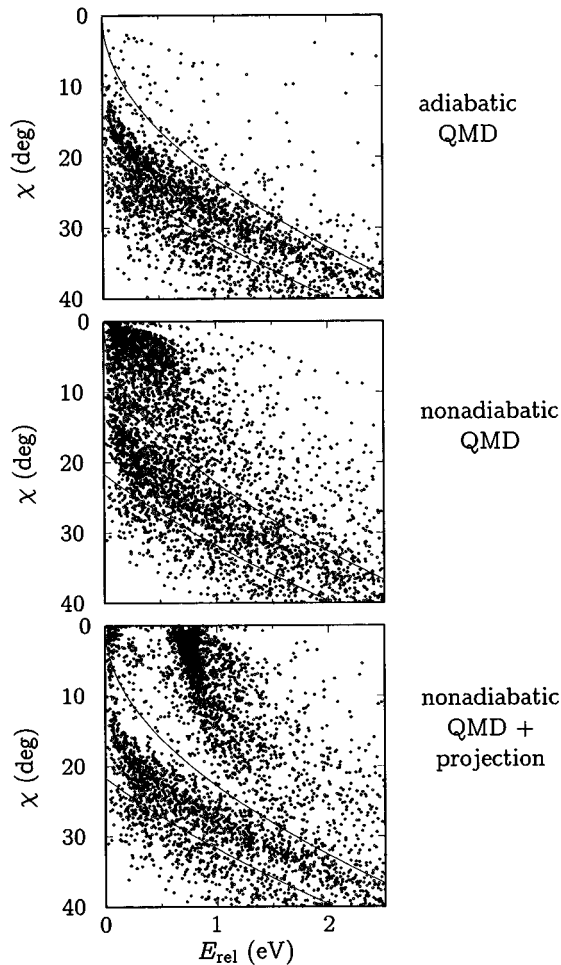


FIG. 11. Calculated distribution of fragmentation events as a function of the relative energy of the fragments E_{rel} and the CM scattering angle χ for collisions $\text{Na}_2^+ + \text{He}$ ($E_{\text{CM}} = 80$ eV, $E_{\text{int}} = 0.2$ eV) in the experimentally measured region [compare to Fig. 3(a)]. From *top* to *bottom*: adiabatic QMD, nonadiabatic QMD, and nonadiabatic QMD including quantum effects on the atomic motion. The lines correspond to the analytical kinematic model for $E_{\text{int}} = 0$ eV (lower) and $E_{\text{int}} = 0.96$ eV (upper).

tion, a finite temperature of the clusters in the beam is taken into account by randomly chosen velocities assuming no electronic excitations and an internal energy of 0.2 eV as estimated from the experimental conditions (see Sec. III A). The evolution of the dimers has been followed after the collision with the helium target (with a typical interaction time $\tau_{\text{coll}} \sim 10$ fs) up to 0.5 ps. Thus the fragmentation dynamics can directly be investigated.

As discussed in Sec. III, the correlation between the scattering angle χ and the relative energy of the fragments E_{rel} reveals important aspects of the fragmentation mechanism. To analyze the different mechanisms and physical effects contributing to the experimentally observed correlation we have performed three different kinds of calculations for the same correlation (Fig. 11): an adiabatic QMD analysis where the fragmentation dynamics is exclusively determined by momentum transfer because the electrons are treated in their ground state (upper part of Fig. 11), an NA-QMD analysis where in addition the electronic mechanism of dissociation is considered (middle part), and an extended NA-QMD analy-

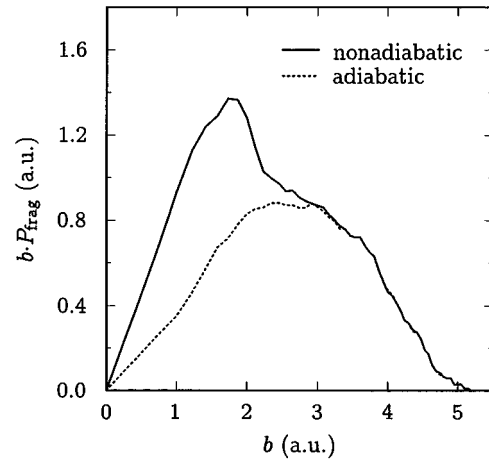


FIG. 12. Calculated fragmentation probability P_{frag} multiplied by the impact parameter b as a function of the impact parameter for collisions $\text{Na}_2^+ + \text{He}$ ($E_{\text{CM}} = 80$ eV, $E_{\text{int}} = 0.2$ eV). Adiabatic (dotted curve) and nonadiabatic (solid curve) QMD calculations are compared. Note that differences between both calculations are restricted to small impact parameters $b < 3$ a.u.

sis where quantum effects of the atomic motion are taken into account (lower part).

The adiabatic QMD reproduces nicely the first maximum (I) at large deflection angles in the experimental correlation [see Fig. 3(a)] supporting the upper given interpretation in terms of the IM leading to these events. In the NA-QMD analysis a second maximum at small angles $\chi < 10^\circ$ appears, resulting obviously from dissociation products according to EM. However, in contrast to the experimental correlation no breakup into two structures [II and III in Fig. 3(a)] is observed. This has a transparent physical interpretation: whereas in the NA-QMD the atomic motion is treated classically the occurrence of the two electronic peaks in the experiment clearly signals that also the atomic dynamics is quantized. Therefore, a full quantum-mechanical treatment of the whole system is required. In the present case, however, one may easily incorporate quantum effects of the relative motion as follows: from the time-dependent wave function $\psi(t)$ of the valence electron one may obtain the occupation probabilities $P_i(t) = |\langle \psi(t) | \psi_i \rangle|^2$ of different eigenstates with the Born-Oppenheimer “surfaces” $E_i(R)$ and the adiabatic wave functions ψ_i (see also Fig. 15). With this probability a potential curve $E_i(R)$ can randomly be chosen right after the interaction with the target. The fragmentation dynamics can then be followed along this eigenstate. The result of this projection is shown in the bottom part of Fig. 11. It nicely reproduces the three maxima in the experimental correlation [Fig. 3(a)].

To gain further insight into the dynamics, the fragmentation probability P_{frag} has been considered as a function of the impact parameter b . It is defined by $P_{\text{frag}}(b) = T_{\text{frag}}(b)/T_{\text{all}}(b)$ with T_{all} the number of calculated trajectories and T_{frag} the number of trajectories where the dimer dissociates. For a fixed b this quantity represents an average over the various initial orientations of the dimer. Figure 12 shows the impact parameter dependence of bP_{frag} , where again NA-QMD calculations are compared with that obtained by QMD calculations. The maximum of the adiabatic

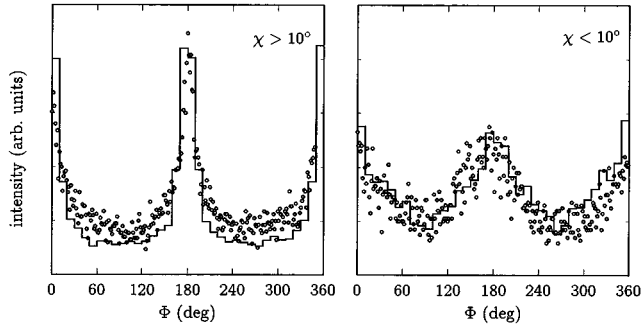


FIG. 13. Calculated intensity (histograms) of fragmentation events as function of the angle Φ for collisions $\text{Na}_2^+ + \text{He}$ ($E_{\text{CM}} = 80$ eV, $E_{\text{int}} = 0.2$ eV) compared to the experimental results (circles) for collisions with large scattering angles $\chi > 10^\circ$ (left panel) and small ones $\chi < 10^\circ$ (right), respectively.

P_{frag} appears at $b \approx 3$ a.u., which is just half of the atomic distance in Na_2^+ of about 6 a.u. Somewhat surprisingly, electronic transitions increase remarkably the nonadiabatic (i.e., total) fragmentation probability for central collisions only. On one side, this means that electronic excitations leading to dissociation must be connected with some momentum transfer. On the other side, these events show up at small angles $\chi < 10^\circ$. Therefore, only very specific orientations of the dimer with respect to the beam axis can contribute to these events. In fact, the further combined theoretical and experimental analysis will justify this expectation.

To elucidate the role of the momentum transfer the so-called Φ correlation (with Φ the angle between the the reaction and dissociation plane, see Fig. 2) will be considered. In a pure IM of dissociation one would expect a strong correlation between the reaction and dissociation plane resulting in strong maxima at $\Phi \sim 0^\circ$ (360°) and 180° , i.e., in-plane fragmentation. In the other extreme case of an ideal EM of dissociation no correlation between both planes is expected. Figure 13 shows the experimental and calculated intensity of the fragmentation events as a function of Φ separated for collisions with $\chi > 10^\circ$ and $\chi < 10^\circ$, respectively. Experimental and theoretical data are found to be in excellent agreement in both cases. As expected, for collisions with large χ (IM) one finds a strong preference of $\Phi \sim 0^\circ$ and 180° for $\chi > 10^\circ$. For small angles $\chi < 10^\circ$ this preference is much less pronounced but still observed, clearly demonstrating that electronic excitations occur in connection with some momentum transfer (central collisions).

One of the questions of interest concerns the relative contribution of the individual electronic states leading to the two maxima (II, III) in the $E_{\text{rel}} - \chi$ diagram. For this purpose the calculated electronic states E_i of Na_2^+ as a function of the atomic distance R are shown in the upper panel of Fig. 14. In the lower panel of Fig. 14 the impact parameter dependence of the mean electronic excitation probability $\bar{P}_i(b)$ obtained by averaging $P_i(t \rightarrow \infty)$ over all collisions with impact parameter b is shown. As discussed above, electronic transitions occur mainly in central collisions $b < 3$ a.u. The dominating channel is the excitation of the (dissociative) $\sigma_u 3s$ level. An interesting feature of this transition is the decrease of $P_{\sigma_u 3s}$ for small impact parameters $b < 1$ a.u., which is connected with the symmetry of the states (for effects on the

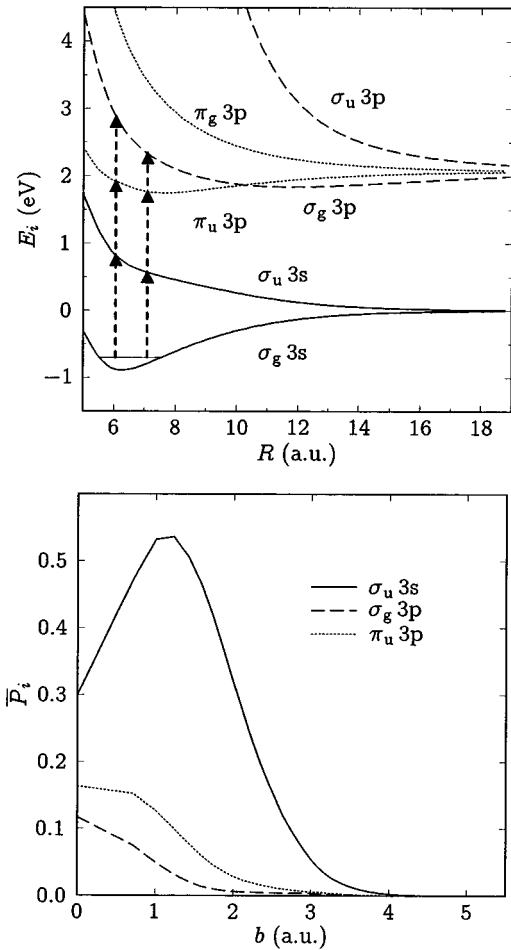


FIG. 14. Top panel: Calculated potential energy curves of Na_2^+ for the lowest levels E_i as a function of the atomic distance R . Symmetries are distinguished by different line styles. The relevant transitions are indicated by bold dashed arrow lines. As the dimers vibrate and electronic transitions can occur at different atomic distances the excitation energy as well as the relative energy of the fragments may vary considerably. Bottom panel: Averaged electronic transition probabilities \bar{P}_i ($i = \sigma_u 3s, \sigma_g 3p, \pi_u 3p$) as a function of the impact parameter b for collisions $\text{Na}_2^+ + \text{He}$ ($E_{\text{CM}} = 80$ eV, $E_{\text{int}} = 0.2$ eV). The transition probabilities into the other states are negligible small. Note the decrease of $P_{\sigma_u 3s}$ for small impact parameters $b < 1$ a.u.

fragmentation dynamics see below). Transitions into the $\pi_u 3s$ and $\sigma_g 3p$ are less probable and those into higher states are negligibly small. Comparing now the energy releases $E_i(R \approx 6-7 \text{ a.u.}) - E_i(R \rightarrow \infty)$ of the contributing states with the experimental kinetic energies E_{rel} of the fragments [see Fig. 3(a)] one clearly concludes that structure II ($E_{\text{rel}} \sim 0.7$ eV) is connected with dissociation events originating from the $\sigma_u 3s$ and $\sigma_g 3p$ levels whereas structure III ($E_{\text{rel}} \sim 0$ eV) results from the weakly bound $\pi_u 3p$ level.

The electronic excitation processes can be further analyzed by investigating the time dependence of the occupation probability P_i . Figure 15 shows $P_i(t)$ and the energy levels $E_i(t)$ for the contributing states (see lower part of Fig. 14) obtained from a typical central collision. The energy of the initially occupied ground state $E_{\sigma_g 3s}(t)$ is shown too. The various transitions can directly be assigned to the couplings

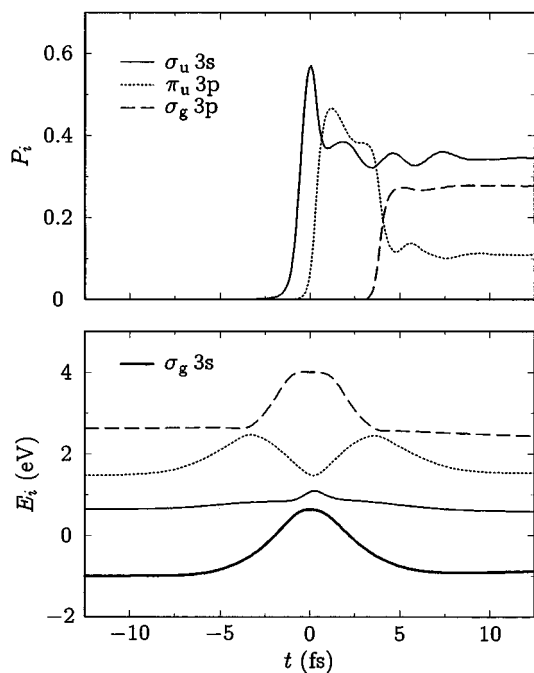


FIG. 15. Calculated time evolution of the energy levels E_i (bottom) and the occupation probabilities P_i (top) of the participating orbitals ($i = \sigma_u 3s$, $\sigma_g 3p$, $\pi_u 3p$) for a typical collision $\text{Na}_2^+ + \text{He}$ ($E_{\text{CM}} = 80$ eV, $b = 0$). Note that electronic transitions correspond to avoided crossings and appear as a multistep process.

(avoided crossings) between the states during the collision (compare upper and lower part of Fig. 15). Direct transitions from the ground state are observed in the $\sigma_u 3s$ and $\pi_u 3p$ levels whereas the excitation of $\sigma_g 3p$ happens indirectly via $\pi_u 3p$. Obviously, this multistep process requires a nonperturbative treatment of the electronic dynamics.

Finally, details of the (different) collision and dissociation geometry of the individual electronic states will be discussed by considering the α correlation. Figure 16 shows the intensity as a function of the angle α for collisions with $\chi < 10^\circ$. Results from measurements and calculations are compared. Whereas the experimental data are separated for structures II and III in Fig. 3, the calculated intensities are distinguished by the excited electronic state. These intensities have been obtained by weighing each trajectory with the probability $P_i(t \rightarrow \infty)$. In the right panel of Fig. 16 one observes a minimum for the experiments at $\alpha = 90^\circ$. This minimum can be understood through the dominating intensity of the $\sigma_u 3s$ state. Its origin is the same as that for the appearance of the

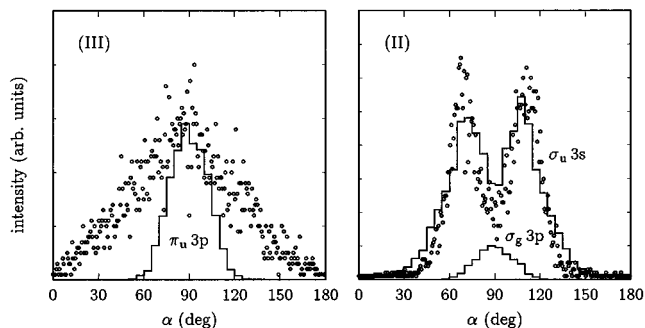


FIG. 16. Calculated intensity (histograms) of fragmentation events resulting from different electronic states as a function of the angle α for collisions $\text{Na}_2^+ + \text{He}$ ($E_{\text{CM}} = 80$ eV, $E_{\text{int}} = 0.2$ eV) with $\chi < 10^\circ$ compared to experimental results (circles). The experimental data on the right and the left correspond to the structures II and III in Fig. 3(a), respectively.

“hole” in $P_{\sigma_u 3s}(b)$ at $b < 1$ a.u. (see Fig. 14). Transitions between gerade and ungerade states are suppressed for nearly symmetry conserving collisions, i.e., central collisions where the dimers are oriented orthogonal to the beam axis ($\alpha \approx 90^\circ$). The opposite is the case for the $\sigma_g 3p$ and $\pi_u 3p$ states, which exhibits maxima at $\alpha \approx 90^\circ$.

V. CONCLUSION

In summary, we have presented a combined experimental and theoretical analysis of CID by applying two novel techniques: kinematic complete correlation experiments and microscopic NA-QMD theory. So, mechanisms of CID in $\text{Na}_2^+ + \text{He}$ collisions have been elucidated in full detail. The experimental analysis of the more complicated $\text{Na}_2^+ + \text{H}_2$ collision shows that the same mechanisms hold simplifying considerably the understanding of such a four-body system. A systematic extension and further applications of the combined experimental and theoretical analysis to larger systems are in progress [19].

ACKNOWLEDGMENTS

The experimental group (Orsay) is indebted to the Laboratoire Aime Cotton (CNRS, Orsay) and the Max Planck Institute (Göttingen) for technical help with the realization of the sodium oven. This work was supported by a E.U. Human Capital and Mobility Program through the Collision-Induced Cluster Dynamics Network under Contract No. CHRX-CT-940643.

- [1] See, e.g., J. Durup, *Recent Developments in Mass Spectrometry*, edited by K. Ogata and T. Hayakawa (University of Tokyo Press, Tokyo, 1970), p. 921; J. Los and T.R. Govers, in *Collision Spectroscopy*, edited by R.G.Cooks (Plenum Press, New York, 1978), p. 289.
- [2] J. Schopmann, P.G. Fournier, and J. Los, *Physica (Amsterdam)* **63**, 518 (1973).
- [3] D.P. de Bruijn and J. Los, *Rev. Sci. Instrum.* **53**, 1020 (1981).

- [4] T.A. Green, *Phys. Rev. A* **1**, 1416 (1970); J.A. Fayeton, A. Pernot, P.G. Fournier, and M. Barat, *J. Phys. (Paris)* **32**, 743 (1971).
- [5] N.R. Zare, *J. Chem. Phys.* **47**, 204 (1967).
- [6] See, e.g., D.P. de Bruijn, J. Neuteboom, V. Sidis, and J. Los, *Chem. Phys.* **85**, 215 (1984); A.B. van der Kamp, R.S. Hiemstra, W.J. van der Zande, R. Fink, and M. Jungen, *J. Chem. Phys.* **99**, 7487 (1993).

- [7] P. Fournier, C. A. van de Runstraat, T.R. Govers, J. Schopmann, F.J. de Heer, and J. Los, *Chem. Phys. Lett.* **9**, 426 (1971).
- [8] D.R. Bates, C.J. Cook, and J.F. Smith, *Proc. Phys. Soc. London* **83**, 49 (1964); B.H. Mahan, *J. Chem. Phys.* **52**, 5221 (1970); Ch. Ottinger and S. Zimmermann, *Chem. Phys.* **53**, 293 (1980).
- [9] J.C. Brenot, H. Dunet, J.A. Fayeton, M. Barat, and M. Winter, *Phys. Rev. Lett.* **77**, 1246 (1996).
- [10] U. Saalman and R. Schmidt, *Z. Phys. D* **38**, 153 (1996).
- [11] R. Campargue, *Rev. Sci. Instrum.* **35**, 111 (1964).
- [12] J.K. Swenson and D. Brandt, *IEEE Trans. Nucl. Sci.* **30**, 1548 (1983).
- [13] S. Kita, K. Noda, and H. Inouye, *J. Chem. Phys.* **63**, 4930 (1975).
- [14] M. Barat, J.C. Brenot, H. Dunet, J.A. Fayeton, D. Madsen, and Y.J. Picard, *The Physics of Electronic and Atomic Collisions: Book of Invited Papers and Progress Reports* (World Scientific, Singapore, in press).
- [15] J.C. Brenot, M. Durup-Ferguson, J.A. Fayeton, K. Goudjil, and M. Barat, *Chem. Phys.* **179**, 549 (1994).
- [16] T.A. Green and J.M. Peek, *Phys. Rev.* **183**, 166 (1969).
- [17] M. Barat, J.C. Brenot, H. Dunet, and J.A. Fayeton, *Z. Phys. D* **40**, 323 (1997).
- [18] M. Barat, J.C. Brenot, H. Dunet, J.A. Fayeton, Y.J. Picard, U. Saalman and R. Schmidt (unpublished).
- [19] U. Saalman and R. Schmidt, *Z. Phys. D* (to be published).